Enhancing the reliability of floating offshore wind turbine towers subjected to misaligned wind-wave loading using tuned mass damper inerters

Renewable Energy 211 (2023) 522–538

Contents lists available at ScienceDirect

Renewable Energy

journal homepage: www.elsevier.com/locate/renene

Enhancing the reliability of floating offshore wind turbine towers subjected to misaligned wind-wave loading using tuned mass damper inerters (TMDIs)

Breiffni Fitzgerald [a,*], James McAuliffe [a], Shubham Baisthakur [a], Saptarshi Sarkar [b]

[a] Department of Civil, Structural and Environmental Engineering, School of Engineering, Trinity College Dublin, Ireland
[b] Department of Mechanics and Maritime Sciences, Chalmers University of Technology, Gothenburg, Sweden

ARTICLE INFO

Keywords:
Inerter
Tuned Mass Damper Inerter (TMDI)
Stochastic wind-wave loads
Spar-type floating offshore wind turbine
Fragility analysis
Reliability

ABSTRACT

Floating offshore wind turbines (FOWTs) are the largest rotating structures on the earth. Dynamically sensitive structures such as these must be protected in these environments to ensure that they can continue to operate reliably and safely. In this paper structural dynamic models and probabilistic assessment tools are combined to demonstrate improvements in structural reliability when FOWT towers are equipped with a new type of damper — the tuned mass damper inerter (TMDI). A multi-body dynamic approach is used to model the wind turbine and the TMDI installed in the tower. The model is subjected to stochastically generated wind and wave loads of varying magnitudes to develop wind-induced probabilistic demand models for towers of FOWTs under model and load uncertainties. A focus is placed on the impact of the wind-wave misalignment on the lightly damped side-to-side mode. Numerical simulations are carried out to construct fragility curves which illustrate reductions in the vulnerability of FOWTs to wind and wave loading owing to the inclusion of the new damper. Results show that the TMDI delivers significant increases in structural reliability of FOWT towers.

1. Introduction

The race to replace fossil fuels with clean sources of energy has been accelerated in the past decade leading to large growth in the wind energy sector. This race is currently fuelled by two key driving components, the first being the 2050 net zero emission goal set out under the Paris Agreement in 2015. In order to achieve this goal, wind generation must increase by at least 18% per year between 2020–2030 [1]. The second driving factor is the cost of energy (COE). In 2020, 62% of the newly installed renewable energy sources produced energy at a COE lower than the cheapest fossil fuel available [2]. This has been made possible by the rapid decline in renewable prices in the last decade, in 2020 alone the IRENA (International Renewable Energy Agency) reported that the average cost of onshore wind production fell by 13% while offshore production costs fell by 9% [2].

The rapid growth in demand for wind energy has led to many new technological developments in wind turbine design. Since wind power production depends on the cube of the inflow wind velocity and the square of the turbine's rotor diameter, there has been exponential growth in the size of the blades and towers of wind turbines. An increase in hub heights allows wind turbines to reach greater wind speeds due to the wind shear effect, while also allowing the space for greater diameter rotors to be fitted. Today's modern multi-megawatt wind turbines are tall slender structures with hub heights exceeding 150 metres and rotor diameters in excess of 240 metres making them the largest rotating structures in the world [3]. There is now a drive to move these structures deeper offshore on floating platforms to expose them to stronger and less turbulent winds.

The increased size of wind turbine blades and towers has led to increasingly slender and flexible structures. The increase in flexibility in addition to the increased wind loads has resulted in wind turbines having a large blade and tower displacements. Introducing hydrodynamic loads and platform motion in addition to aerodynamic loads has led to instabilities in wind turbines introducing large vibrational responses. Dueñas-Osorio and Basu [4] showed the extent to which these vibrational responses can decrease the availability of wind turbines with implications for power production and LCOE. In addition to reduced power production, accelerations experienced by turbine towers can cause damage to sensitive components in the nacelle leading to large downtime, in particular for offshore wind turbines where repair access is limited.

Many studies have investigated the installation of TMDs in wind turbine blades and towers to mitigate vibration [5–12]. Despite encouraging results, the large mass ratios required and lack of adaptability make TMDs an unideal vibration controller for offshore wind turbines [13]. A wide array of different dampers have been investigated

* Corresponding author.
E-mail addresses: breiffni.fitzgerald@tcd.ie (B. Fitzgerald), jmcaulif@tcd.ie (J. McAuliffe), baisthas@tcd.ie (S. Baisthakur), ssarkar@chalmers.se (S. Sarkar).

https://doi.org/10.1016/j.renene.2023.04.097
Received 21 November 2022; Received in revised form 17 April 2023; Accepted 18 April 2023
Available online 29 April 2023

in recent years such as active TMDs [14–16], semi-active TMDs [17] and tuned liquid column dampers [18–20] to name a few.

A novel damping device, which has been proposed in several recent studies for FOWT vibration control is the Tuned Mass Damper Inerter (TMDI). The TMDI which was first introduced by Smith [21] in 2002 is a new variant of the classical TMD. The TMDI works by including an inerter in addition to the spring and damper in a classical TMD system. The inerter is a mechanical device that converts linear motion into high-speed rotational motion in a flywheel. This results in an amplifying effect of the mass of the TMD. The presence of the inerter virtually increases the mass of the damper leading to greater vibration control capabilities without the burden of increasing the mass ratio. The inerter enables one to achieve improved vibration control using a fixed mass ratio or equal structural control using a lighter damper — which is particularly beneficial for large flexible structures such as FOWTs.

In 2014 Marian [22] proposed governing equations for the optimal design of a TMDI fitted in a stochastically support-excited structural system that can be utilised in floating offshore wind turbines. The research also suggests that smaller mass ratios (less than 3%) are capable of producing larger response reductions than TMDIs with larger mass ratios.

Hu et al. [23] employed an inerter-based dynamic vibration absorber (IDVA) in an attempt to mitigate wind loads experience by wind turbines. The results of the research found that the IDVA was capable of reducing the wind loads experienced by the wind turbine system under various rotational frequencies. In a later paper, Hu et al. [24] used a TMDI damping device to investigate load mitigation in barge-type floating offshore wind turbines. The results showed that there is a trade off between fore-aft tower deflections and TMD stroke space. However, for a given stroke space a TMDI will have increased structural control.

Ma et al. [25] used H_2 optimisation in order to find the optimal parameters for a tuned heave plate with the addition of an inerter in a semi-submersible platform. Ma also proposed a novel inerter consisting of a small waterwheel. The novel THPI was seen to reduce the heave motion by 19% while the novel waterwheel inerter produced large apparent masses in comparison with traditional mechanical devices. Sarkar et al. [26] investigated the influence of a TMDI on the vibrational response of a spar-type offshore wind turbine. Significant reductions in both tower fore-aft and side-to-side directions were observed while large reductions of up to 90% in the TMDI's stroke were observed. Zhang et al. [27] proposed the use of tuned parallel inerter mass systems (TPIMS) as retrofitting devices in wind turbines in an attempt to mitigate large seismic responses, the response of the tower and hence the tower base shear and bending moments are significantly reduced by introducing a TMDI to the system. Villoslada et al. [28] used NREL's FAST SC software to install a TMDI in the nacelle of NREL's 5 MW wind turbine supported by a barge-type platform. The results showed that the introduction of the TMDI had a significant improvement of the fatigue life of the turbine.

Zhang et al. [29] implemented the Euler–Lagrangian approach to construct a multi-modal model of a modern multi-megawatt wind turbine. Damping devices consisting of a TMD and TMDI were placed close to the tip of the three wind turbine blades and closed-form expressions were derived to calculate the optimal tuning and damping ratios of the damping devices. Zhang et al. [30] conducted a similar study with an alternative damping device, the RIDTMD, this device proposed by Garrido et al. [31], is similar to a traditional TMD however the dashpot is replaced with a tuned viscous mass damper (TVMD). The RIDTMD provided significant reductions in edgewise blade vibrations in comparison with the conventional TMD at the expense of a slight increase in the damper stroke. Zhang et al. [32] extended their research on the RIDTMD by implementing a RIDTMD in the nacelle of a spar-type floating offshore wind turbine. This model utilised a 6-degree-of-freedom model to perform a parameter optimisation. The optimised damping device is then compared with an optimal TMD. The RIDTMD is observed to outperform the TMD in reducing the side-to-side displacements of the tower, however, the TMD had a slightly decreased stroke.

In a later paper, Zhang et al. [33] proposed an ungrounded tuned mass inerter system (TMIS) for vibration mitigation of wind turbine towers. The TMIS consists of a mass, spring and an inerter subsystem. By testing the device on a 1.5 MW wind turbine the device was proven to provide reduced vibration responses at a given device mass. Chen et al. [34] performed numerical simulations on NRELs 5MW fixed-based wind turbine with an inerter-based dynamic vibration absorber in the nacelle (IDVA). The results demonstrated that smaller mass ratios in the IDVA can achieve the same control in comparison to traditional TMDs.

Sun et al. [35] implemented an inerter-based point absorber (IPA) in a wave energy converter (WEC) which is fixed to the tower of NREL's 5MW Monopile-based offshore wind turbine. Optimal parameters for the IPA were obtained using analytical expressions. The IPA WEC was seen to have greater energy absorption in comparison with a traditional point absorber. The IPA demonstrated an ability to operate over a wider range of wave peak frequencies increasing its operational bandwidth and hence energy absorption.

Sarkar and Fitzgerald [36] proposed the use of a tuned mass damper fluid inerter in a spar-type floating offshore wind turbine in order to mitigate the vibrational response of the tower. The fluid inerter due to its simplistic design and low maintenance costs can reduce downtimes experienced by wind turbines with mechanical inerters. The TMDFI greatly outperforms traditional TMDs while rivalling the performance of traditional inerters.

In this paper, a tuned mass damper inerter (TMDI) is installed in the tower of a spar-type FOWT. Previous work by the authors has shown that inerter-based TMDs have great potential in vibration control of FOWTs where enhanced vibration mitigation can be achieved using a relatively lighter device [26,36]. However, the work presented in [26,36] offered a deterministic evaluation of the capability of the TMDI. A probabilistic evaluation of the damper performance subjected to different limit states is unexplored. In this paper, we address this gap by examining the improvement in structural reliability that can be achieved when a TMDI is installed in the tower of a FOWT. The reliability of the FOWT is assessed by performing a fragility analysis of the turbine. Fragility analysis utilises a probabilistic approach which assesses the demand of a structure with respect to limit states such as displacements, accelerations or loads. Recent studies have utilised fragility analysis to present the structural reliability of wind turbines in a stochastic sense [16,37–46]. Particular attention is paid to misaligned wind-wave loading which can excite the structure in its less damped side-to-side mode.

Based on the literature presented above, this paper:

- Proposes a probabilistic methodology to evaluate TMDIs in FOWT towers
- Demonstrates improvements in FOWT tower reliability when tuned mass damper inerters (TMDIs) are installed.
- Examines the effect of misaligned wind-wave loading on the less damped side-to-side tower mode in FOWTs in numerical simulations.

Results indicate that the TMDI reduces the probability of exceeding a given displacement limit for all examined met ocean conditions and thus it improves the reliability of the tower response even in misaligned conditions. The TMDI significantly improves the wind-induced fragility of FOWT towers. For equal damper mass a TMDI is more effective than traditional dampers.

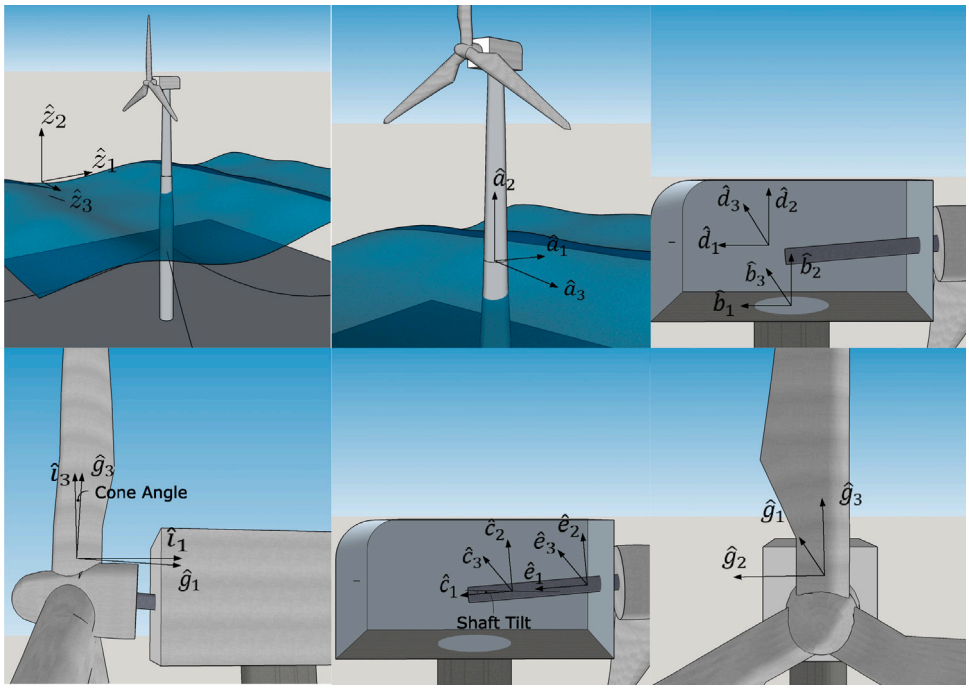

Fig. 1. Coordinate systems for FOWT.

2. Floating offshore wind turbine coupled with TMDI

A nonlinear aeroelastic multi-body dynamic model of a floating offshore wind turbine (FOWT) is used in this study to examine the effectiveness of TMDIs at reducing FOWT tower vibration and improving FOWT tower reliability when subjected to stochastic wind-wave loading environments. This model has been developed previously by the authors, see [47] for details. The full nonlinear FOWT model has 22 degrees of freedom (DOFs), as listed in Appendix A. Aerodynamic and hydrodynamic loads on the wind turbine are estimated using blade element momentum (BEM) theory and Morison's equation, respectively. The mooring cables are modelled using MoorDyn [48]. For brevity, details on the dynamic modelling of the 22-DOF system are not presented in this work. The reader will find more details on the modelling in [47]. The model has been developed using Kane's method [49], Fig. 1 shows the FOWT with coordinate systems defined that are used by Kane's approach to derive equations of motion.

By a direct result of Newton's law of motion, Kane's equations of motion for a simple holonomic multi-body system can be stated as [49]

$$F_k + F_k^* = 0 \qquad \text{for } k = 1, 2, \dots N \tag{1}$$

where N is the total number of degrees of freedom required to describe the complete kinematics of the FOWT system. With a set of M rigid bodies characterised by reference frame N_i and centre of mass point X_i, the *generalised active force* associated with the kth degree of freedom is given by [49]

$$F_k = \sum_{i=1}^{M} \left[{}^{E}\mathbf{v}_k^{X_i} \cdot \mathbf{F}^{X_i} + {}^{E}\boldsymbol{\omega}_k^{N_i} \cdot \mathbf{M}^{N_i} \right] \tag{2}$$

where $\mathbf{F}^{X_i}$ is force vector acting on the centre of mass of point X_i and $\mathbf{M}^{N_i}$ is the moment vector acting on the N_i rigid body. ${}^{E}\mathbf{v}_k^{X_i}$ and ${}^{E}\boldsymbol{\omega}_k^{N_i}$ are the partial linear and partial angular velocity of the point X_i and rigid body N_i respectively associated with the kth degree of freedom in the inertial (E) reference frame. The *generalised inertia force* for kth degree of freedom is given as

$$F_k^* = -\sum_{i=1}^{M} \left[{}^{E}\mathbf{v}_k^{X_i} \cdot \left(m^{N_i} {}^{E}\mathbf{a}^{X_i} \right) + {}^{E}\boldsymbol{\omega}_k^{N_i} \cdot {}^{E}\dot{\mathbf{H}}^{N_i} \right] \tag{3}$$

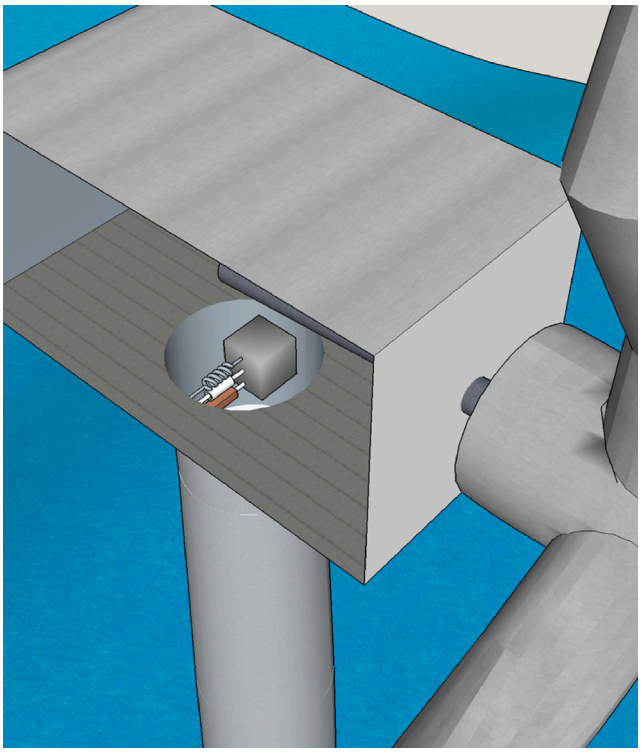

Fig. 2. Floating offshore wind turbine with TMDI.

where it is assumed that for each rigid body N_i, the inertia forces are applied at the centre of the mass point X_i. ${}^{E}\dot{\mathbf{H}}^{N_i}$ is the time derivative of the angular momentum of the rigid body N_i about its centre of mass X_i in the inertial frame [49]. For the FOWT model, the mass of the platform, tower, yaw bearing, nacelle, hub, blades and generator contribute to the total generalised inertia forces. Generalised active forces are the forces applied directly to the FOWT system, forces that

ensure constraint relationships between the various rigid bodies and internal forces within flexible members. Forces applied directly on the FOWT system include aerodynamic forces on the blades and the tower, hydrodynamic forces on the platform, mooring forces on the platform, gravitational forces, generator torque forces and the high-speed shaft brake. Gearbox friction forces have not been considered in this model. Yaw springs and damper contribute to forces that enforce the constraint relationship between rigid bodies. Internal forces within flexible members include elasticity and damping in the tower, blades and drivetrain [50].

In this work a tuned mass damper inerter (TMDI) has been installed in the tower of the FOWT, the damper is placed at the tower-top as shown in Fig. 2. The inclusion of the damper increases the degrees of freedom in the model to 23. The incorporation of an auxiliary damping device, i.e. a TMD or TDMI, into the FOWT model is quite straightforward using Kane's approach. It is evident from Eqs. (1) - (3) that defining the kinematic description, i.e., the position, velocity and acceleration vectors of all important points on the FOWT, is the key requirement for modelling. Hence, one needs only to define the position vector of the damper from the tower top to incorporate the damper into the model. This position vector can be given as

$$r^{OD} = \begin{cases} q_D \hat{\mathbf{b}}_3 & \text{coupled to side-to-side direction} \\ q_D \hat{\mathbf{b}}_1 & \text{coupled to fore-aft direction} \end{cases} \tag{4}$$

where D denotes the centre of mass of the damper and q_D is the displacement of the damper from its neutral position. The mass of the damper contributes to the generalised inertia forces and the spring, damper and inerter contribute to the generalised active forces of the entire system. To describe the complete motion of the coupled FOWT-TMDI system the degrees of freedom/generalised coordinates used are provided in Eq. (5).

$$\begin{aligned} \mathbf{q} = \{ & q_{Sg} \;\; q_{Sw} \;\; q_{Hv} \;\; q_R \;\; q_P \;\; q_Y \;\; q_{TFA1} \;\; q_{TSS1} \;\; q_{TFA2} \\ & q_{TSS2} \;\; q_{yaw} \;\; q_{GeAz} \;\; q_{DrTr} \\ & q_{B1F1} \;\; q_{B1E1} \;\; q_{B1F2} \;\; q_{B2F1} \;\; q_{B2E1} \;\; q_{B2F2} \;\; q_{B3F1} \;\; q_{B3E1} \;\; q_{B3F2} \;\; q_D \} \end{aligned} \tag{5}$$

The subscripts define the degrees of freedom under consideration and are described in Appendix A. Once the linear and angular velocity vectors for every important point and rigid body in the system are defined, the partial linear and angular velocities are obtained as per [49] using the time derivatives of the generalised coordinates as the generalised speed (i.e., $u_k = \dot{q}_k$). The complete non-linear time-domain equations of motion for the FOWT in its general form can be written as

$$\mathbf{M}(\mathbf{q}, \mathbf{u}, t)\dot{\mathbf{q}} = -\mathbf{f}(\dot{\mathbf{q}}, \mathbf{q}, \mathbf{u}, t) \tag{6}$$

where, $\mathbf{M}$ is the inertial mass matrix that is a non-linear function of the set of degrees of freedom $\mathbf{q}$, control input $\mathbf{u}$, and time t. The force vector $\mathbf{f}$ depends non-linearly on the degrees of freedom, the time derivative of the degrees of freedom, control input and time.

For more details of the derivation of the multi-body FOWT model see previous works by the authors [26,47,50]. The FOWT model without the coupled damper has been benchmarked and verified against the National Renewable Energy Laboratory's (NREL) fully coupled nonlinear simulation code, OpenFAST [51] in [47].

3. Vibration control of 5-MW FOWT tower — numerical simulations

The nonlinear aeroelastic multi-body dynamic FOWT model is instantiated with details from NREL's 5 MW OC3-Hywind spar-type offshore reference wind turbine. This FOWT is defined in [52] while the spar platform is defined in [53]. The main properties of the considered wind turbine model are provided in Table 1.

Simulations are performed for three cases: without a tower damper, with a classical TMD installed at the top of the tower, and with a TMDI installed at the top of the tower. The response of the structure in each situation was compared and used to generate fragility curves to perform reliability analysis. The non-linear numerical system was solved in MATLAB® [54] utilising the Runge–Kutta 'ODE 4' method.

3.1. TMD tuning parameters

The dampers are tuned to mitigate tower vibration in the less damped side-to-side direction. Vibration in this mode is particularly sensitive to the effects of wind-wave misalignment. The TMD is tuned to the FOWT tower's natural frequency in the side-to-side direction, 0.312 Hz, with a tuning ratio of $\nu_{TMD} = 1.0$. There are many approximate and empirical expressions available in the literature for the evaluation of the optimal damping ratio of a TMD such as those formulated by Ghosh and Basu [55] and Hoang et al. [56]. In this paper the following expression given by Luft [57] for optimal TMD damping is used:

$$\xi_{TMD} = \frac{\sqrt{\mu_{TMD}}}{2} \tag{7}$$

where ξ_{TMD} is the TMD damping ratio and μ_{TMD} is the mass ratio of the TMD. In this study a TMD mass ratio of 1% is used with respect to the tower mass.

3.2. TMDI tuning parameters

In previous work, Sarkar and Fitzgerald [26] developed closed-form expressions for optimum tuning and damping parameters for TMDIs installed in FOWT towers. Considering the TMDI, let μ be the mass ratio and β the inerter ratio defined as

$$\mu = \frac{m_d}{m_0} \qquad \beta = \frac{b}{m_0} \tag{8}$$

where m_d is the TMDI mass and b is the inertance [22], which has the units of mass [22,29,58]. The tuning ratio and damping ratio of the damper are defined as

$$\omega_r = \frac{\omega_d}{\omega_t} \qquad \zeta_d = \frac{c_d}{2 m_d \omega_d} \tag{9}$$

where ω_t and ω_d are the natural frequency of the tower and the TMDI respectively, and c_d is the damping coefficient of the TMDI. The normalised (normalised to 1) displacement of the tower at a height H_I from its base can be obtained directly from the primary mode shape as

$$\phi = \phi_t(H_I) \qquad \text{where } 0 \le \phi \le 1 \tag{10}$$

where ϕ_t is the primary mode shape of the tower, see the schematic in Fig. 3 for details.

The optimum tuning parameters for this system were obtained by Sarkar and Fitzgerald [26] as:

$$\omega_r = \sqrt{\frac{-B + \sqrt{B^2 - AC}}{2A}} \tag{11}$$

where

$$\begin{aligned} A = {} & 3\mu^2(\mu^2 + 2\mu\phi^2\beta - 4\mu\phi\beta + 2\mu\beta + 2\mu + \phi^4\beta^2 \\ & - 4\phi^3\beta^2 + 6\phi^2\beta^2 + 2\phi^2\beta - 4\phi\beta^2 \\ & - 4\phi\beta + \beta^2 + 2\beta + 1) \\ B = {} & \mu(4\mu^2\zeta_d^2 - \mu^2 + 4\mu\phi^2\zeta_d^2\beta - 2\mu\phi^2\beta \\ & - 8\mu\phi\zeta_d^2\beta + 2\mu\phi\beta + 4\mu\zeta_d^2\beta + 4\mu\zeta_d^2 - 2\mu\beta \\ & - 2\mu - \phi^2\beta^2 + 2\phi\beta^2 \\ & - \beta^2 - 2\beta) \\ C = {} & -(\mu^2 + 2\mu\beta + \beta^2) \end{aligned}$$

Table 1
Properties of NREL 5-MW OC3-Hywind spar-type FOWT [52].

NREL 5-MW OC3-Hywind spar-type FOWT properties		
Basic description	Max. rated power	5-MW
	Rotor orientation, configuration	Upwind, 3 blades
	Rotor diameter	126 m
	Hub height	90 m
	Cut-in, rated, cut-out wind speed	3 m/s, 11.4 m/s, 25 m/s
	Cut-in, rated rotor speed	6.9 rpm, 12.1 rpm
Blade	1st in-plane mode natural frequency	1.0606 Hz
	1st out-of-plane mode natural frequency	0.6767 Hz
	Structural-damping ratio(all modes)	0.48%
Tower	1st Fore-Aft mode natural frequency	0.324 Hz
	1st Side-to-Side mode natural frequency	0.312 Hz
	Structural-damping ratio(all modes)	1%

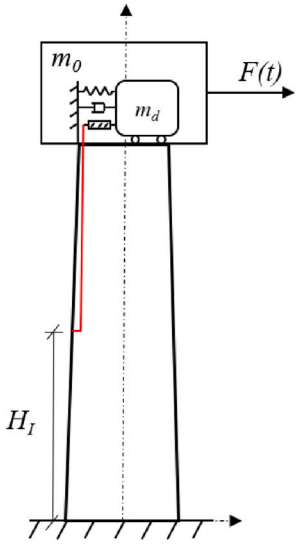

Fig. 3. Schematic diagram of a tower with a TMDI placed on the top.

The optimal damping ratio is given by:

$$\zeta_d = \frac{1}{2\mu\omega_r}\sqrt{\frac{D}{E}} \tag{12}$$

where

$$\begin{aligned} D = {} & \mu^4\omega^4 + 2\mu^3\phi^2\beta\omega_r^4 - 4\mu^3\phi\beta\omega_r^4 + 2\mu^3\beta\omega_r^4 + 2\mu^3\omega_r^4 - \mu^3\omega_r^2 + \mu^2\phi^4\beta^2\omega_r^4 \\ & - 4\mu^2\phi^3\beta^2\omega_r^4 + 6\mu^2\phi^2\beta^2\omega_r^4 + 2\mu^2\phi^2\beta\omega_r^4 - 2\mu^2\phi^2\beta\omega_r^2 - 4\mu^2\phi\beta^2\omega_r^4 \\ & - 4\mu^2\phi\beta\omega_r^4 + 2\mu^2\phi\beta\omega_r^2 + \mu^2\beta^2\omega_r^4 + 2\mu^2\beta\omega_r^4 - 2\mu^2\beta\omega_r^2 + \mu^2\omega_r^4 - 2\mu^2\omega_r^2 + \mu^2 \\ & - \mu\phi^2\beta^2\omega_r^2 + 2\mu\phi\beta^2\omega_r^2 - \mu\beta^2\omega_r^2 - 2\mu\beta\omega_r^2 + 2\mu\beta + \beta^2 \end{aligned}$$

$$E = \mu + \phi^2\beta - 2\phi\beta + \beta + 1$$

It has been shown that these tuning parameters are capable of damping out the energy associated with the tower's natural frequency almost completely. Therefore, these optimal expressions are used to tune the TMDIs in this study. For FOWTs it is not ideal to simply increase the mass of the damper to attain better performance. The increased mass on top of the tower can destabilise the platform and cause excessive vibrations [26]. Therefore, in this paper, the total TMDI mass is ≈ 1% of the mass of the tower, i.e. the same as the mass of the TMD described in Section 3.1. It should be noted that Eqs. (11) and (12) reduce to the optimal tuning parameters for classical TMD(s) when $b = \beta = 0$ and the primary structure is excited by white noise.

3.3. Numerical simulations — design of experiment

A total of 40 wind speeds are selected as intensity measures to produce fragility curves, surpassing Yuan's recommended 36 intensity measures [37] to provide a 95% confidence interval. The 40 wind speeds were selected using Latin Hypercube Sampling (LHS) between the values of 3 m/s and 25 m/s, the cut-in and cut-out wind speeds of the 5-MW FOWT respectively [52]. 25 wind files are generated with turbulence intensities of 0% and 10% for each of the wind speeds (50 files per wind speed). The wind files are generated using TurbSim [59] a package distributed by NREL with each wind file being allocated a unique random seed. TurbSim utilises spatial coherence and wind shear to generate turbulent 3-D wind fields. The International Electrotechnical Commission's (IEC) Normal Turbulence Model (NTM) [60] is used to model atmospheric turbulence. Blade Element Momentum (BEM) theory [61] is then used with the turbulent wind file and the blade and tower geometries to estimate the aerodynamic loads on the blades and the tower.

Six different met-ocean scenarios are considered to produce environmental loading conditions which can be seen in Table 2. The scenarios model calm, moderate and rough met-ocean conditions. These conditions are applied to the FOWT with both aligned and misaligned wind-wave loading. The wave files are computed using linear Airy wave theory with the stochastic sea modelled using the Pierson–Moskowitz spectrum [62]. Morison's equations are implemented to estimate the hydrodynamic forces acting on the spar and tower while the open-source software MoorDyn [48] is used to calculate forces acting on the mooring cables.

To account for variation in material properties and construction techniques a modification factor ranging from 0.97 to 1.03 (3% coefficient of variation), characterised by a uniform random variable, is applied to the elastic modulus of the tower following [19].

For each environmental condition, numerical simulations are run for three different cases: no damper (baseline uncontrolled), with an optimally tuned classical TMD, and with an optimally tuned TMDI. The TMD and TMDI were both assigned mass ratios of 1%. The TMDI is assigned an inertance of $\beta = 0.4$ since it has been shown that the vibration control performance of TMDIs becomes saturated at inerter ratios greater than 0.4 [26].

A total of 36 000 numerical simulations are carried out (40 wind speeds × 25 random seeds/Elastic moduli × 2 turbulence intensities × 6 wave conditions × 3 vibration control situations). The simulation duration is selected as 225 s with the first 75 s removed in order to eliminate the effect of the initial transient phase. The maximum side-to-side tower displacement during the time history is recorded for each of the conditions.

Table 2
Met-ocean conditions.

Wave Conditions				
Load case		Significant Height, Hs (m)	Peak Period, Tp (s)	Wind-Wave Misalignment
LC1	Calm Sea Aligned	0.75	6	0°
LC2	Calm Sea Misaligned	0.75	6	90°
LC3	Moderate Sea Aligned	2.25	6.25	0°
LC4	Moderate Sea Misaligned	2.25	6.25	90°
LC5	Rough Sea Aligned	6	8	0°
LC6	Rough Sea Misaligned	6	8	90°

3.4. Fragility analysis

Fragility curves for each environmental loading condition are produced following an approach developed by Baker [63], with the fragility function defined as:

$$\mathbf{p(C|IM = x)} = \Phi\left(\frac{ln(x/\theta)}{\beta_f}\right) \tag{13}$$

where $\mathbf{p(C|IM = x)}$ is the probability that x, an environmental loading condition, will cause the FOWT to exceed C, a defined limit state. In Eq. (13), Φ is the normal cumulative distribution function, θ and β_f are the fragility parameters; the median of the fragility function and the standard deviation of $ln(IM)$ respectively. The intensity measures IM in this case is the wind speed.

The Maximum Likelihood Estimation (MLE) is used to find the best estimate of the fragility parameters [63]:

$$\mathbf{Likelihood} = \prod_{j=1}^{m}\binom{n_j}{z_j} p_j^{z_j}(1-p_j)^{n_j-z_j} \tag{14}$$

$\prod$ is the product of the sequence, m is the number of wind speeds, n_j is the number of wind files, and z_j is the number of wind files where the limit state is exceeded.

By substituting Eq. (13) into Eq. (14) the following formula is produced:

$$\mathbf{Likelihood} = \prod_{j=1}^{m}\binom{n_j}{z_j} \times \Phi\left(\frac{ln(x_j/\theta)}{\beta_f}\right)^{z_j} \times \left[1-\Phi\left(\frac{ln(x_j/\theta)}{\beta_f}\right)^{(n_j-z_j)}\right] \tag{15}$$

By maximising the likelihood function, the best estimate of the fragility parameters can be obtained:

$$\hat{\theta}, \hat{\beta}_\mathbf{f} = \underset{(\theta,\beta_f)}{argmax} \sum_{j=1}^{m}\left\{ ln\binom{n_j}{z_j} + z_j\ ln\ \Phi\left(\frac{ln(x_j/\theta)}{\beta_f}\right) + (n_j - z_j)\ ln\ \left[1-\Phi\left(\frac{ln(x_j/\theta)}{\beta_f}\right)\right]\right\} \tag{16}$$

The Confidence Intervals can then be formed for the Fragility curves using Eq. (17), which Trevlopoulos et al. [64] suggested as a simplistic formula for the estimation of the error bounds of the confidence interval:

$$\mathbf{E} = \Phi^{-1}(0.025)\left(\sqrt{\frac{P_f(IM)(1-P_f(IM))}{n}}\right), \quad \Phi^{-1}(0.975)\left(\sqrt{\frac{P_f(IM)(1-P_f(IM))}{n}}\right) \tag{17}$$

Φ is the cumulative density function of the standard normal distribution and n is the number of samples computed for the given IM level. The error bounds can be calculated and added to the MLE at each respective wind speed thus giving the 95% confidence interval of the fragility curve.

Table 3
Limit States (Rotation in degrees about Roll DOF).

Limit States					
Load Case	Met-Ocean Conditions	LS1	LS2	LS3	LS4
LC1	Calm Sea Aligned	0.03°	0.04°	0.05°	0.06°
LC2	Calm Sea Misaligned	0.06°	0.07°	0.08°	0.09°
LC3	Moderate Sea Aligned	0.03°	0.04°	0.05°	0.06°
LC4	Moderate Sea Misaligned	0.06°	0.07°	0.08°	0.09°
LC5	Rough Sea Aligned	0.03°	0.04°	0.05°	0.06°
LC6	Rough Sea Misaligned	0.30°	0.31°	0.32°	0.33°

3.4.1. Limit state selection for fragility analysis

The 36,000 numerical simulations produce a wide range of maximum displacement results. Large differences in displacement values between various environmental conditions, such as calm met-ocean conditions with aligned wind-wave loading (LC1) and rough met-ocean conditions with misaligned wind-wave loading (LC6), make it difficult and not very enlightening to define a single set of limit states across the entire range of conditions. By attempting this, fragility curves with 0% or 100% chance of limit state exceedance across the full range of wind speeds are produced for many cases. By producing fragility curves with either 0% or 100% chance of limit state exceedance, the effects of the dampers can be disguised. In order to avoid this, a set of limit states has been selected for each of the environmental conditions (LC1–LC6). These sets of limit states seen in Table 3, contain displacement values that are appropriate for the displacement ranges experienced in each of the environmental conditions. This selection of limit states has been carried out for illustrative purposes, hence allowing the fragility curves to demonstrate the performance of the TMD and TMDI.

3.5. Fragility curves

The resulting fragility curves are presented in Figs. 4–7. The fragility curves have been analysed at sample wind speeds of 11.4 m/s (rated wind speed) and 15 m/s in order to demonstrate the performance of the dampers operating at typical wind speeds. These results are presented in Tables 4–9. In these tables, we present percentage reduction values. These are percentage reductions of the FOWT tower fragility for the TMD and TMDI-controlled cases when compared to the uncontrolled case. It should be noted that the fragility curves produced from steady-state wind conditions with low vibrational responses are influenced highly by Young's modulus variation, particularly at lower limit states. As a result, fragility curves produced by these conditions may be influenced more by Young's modulus rather than the effects of damping devices.

Table 10 illustrates the reduction in maximum displacements values at the tower top as a result of the damping devices. Again, these values are percentage reduction values comparing the TMD and TMDI-controlled cases to the uncontrolled case.

Table 11 allows us to assess the impact that the misalignment of wind-wave conditions has on the turbine tower. This table compares the percentage increase of the maximum displacement experienced by the

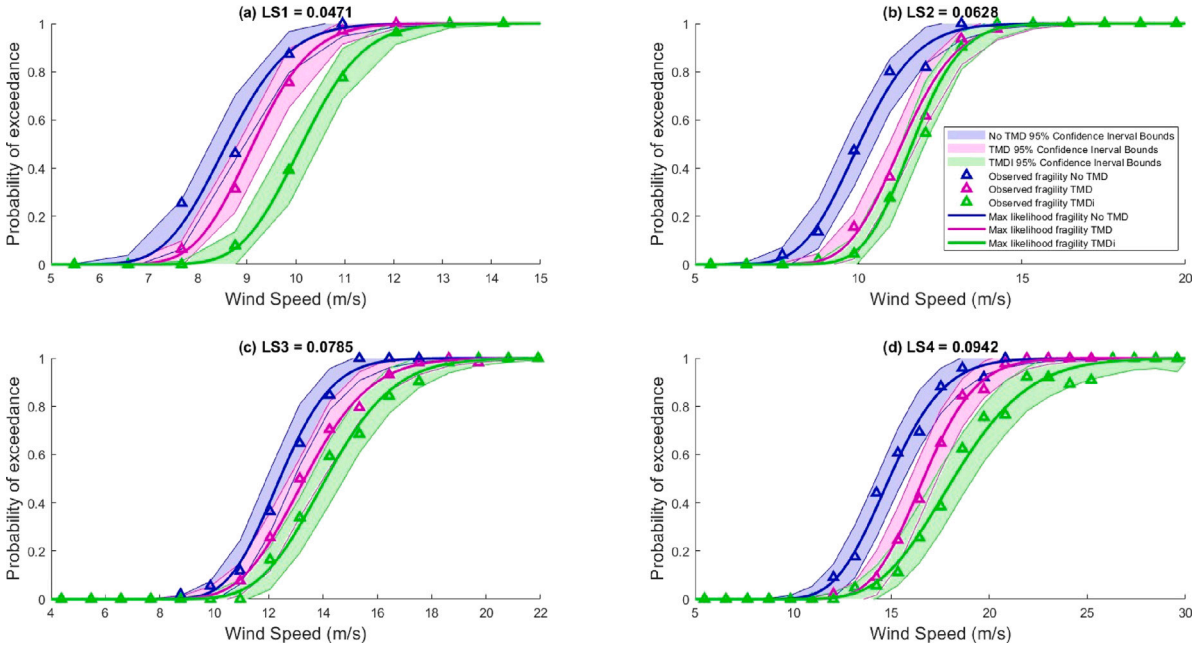

Fig. 4. LC1, Calm met-ocean conditions, 10% turbulence intensity, Aligned wind-wave loading, Wave significant height (0.75 m), Peak wave period (6 s).

Table 4
Percentage reductions in probability of limit state exceedance by controllers vs uncontrolled: Calm Met-ocean conditions, Aligned Wind and Wave.

Calm Met-ocean conditions Aligned Wind and Wave					
	Controller	LS1 (%)	LS2 (%)	LS3 (%)	LS4 (%)
11.4 m/s, 0% Turb	BaseLine	–	–	–	–
	TMD	69.92	−0.74	0.10	0
	TMDI	95.13	−4.84	0.10	0
11.4 m/s, 10% Turb	BaseLine	–	–	–	–
	TMD	0.79	30.16	10.82	0
	TMDI	10.32	40.81	17.99	0
15 m/s, 0% Turb	BaseLine	–	–	–	–
	TMD	0	1.44	7.92	0
	TMDI	0	13.83	7.92	0
15 m/s, 10% Turb	BaseLine	–	–	–	–
	TMD	0	0.59	14.12	0
	TMDI	0.0023	0.41	26.95	0

turbine tower across the full range of wind speeds when the wind-wave loadings are aligned in comparison to when they are misaligned.

In Table 11 wave conditions which differ only in wind-wave alignment are compared (LC1 with LC2, LC3 with LC4, LC5 with LC6). The comparison is carried out for 0% and 10% wind turbulence intensities for uncontrolled (Baseline), TMD and TMDI-controlled cases.

Fig. 8 displays time histories of the tower top displacements at a wind speed of 11.0142 m/s (close to rated wind speed) with 10% turbulence intensity. The time histories compare the uncontrolled case, with the TMD and TMDI-controlled cases. Time histories are shown for LC2, LC3, LC4 and LC6 for 100–200 s to illustrate the performance of the dampers and the influence of wind-wave misalignment.

Fig. 9 displays the power output time history of the turbine at a wind speed of 11.0142 m/s with 10% turbulence intensity. The time histories compare the uncontrolled case, with the TMD and TMDI-controlled cases. These time histories are again shown for LC2, LC3, LC4 and LC6 for 100–200 s to illustrate the influence of wind-wave misalignment and any effects that the dampers have on power fluctuations.

4. TMDI performance assessment

Fig. 8 demonstrates the effects of the TMDI and TMD on the response of the FOWT tower. The TMD and TMDI can be seen to greatly reduce and smoothen responses with the TMDI producing larger mitigation capabilities than the TMD. These reductions can be seen in some capacity across all environmental conditions and will heavily influence the fragility curves produced from these responses.

During calm met-ocean conditions with aligned wind and wave loading (LC1) the response of the structure is relatively small. As the dampers operate based on the response of the structure their true potential is not realised here. Despite this, in Fig. 4 the dampers can be seen to shift the fragility curves to the right, hence improving the FOWT tower reliability over a range of wind speeds. The TMD provides a good reduction in the fragility of the FOWT tower with the TMDI improving this further. As presented in Table 4, for a given limit state and a wind speed of 11.4 m/s, the TMDI can be seen to decrease fragility by 40.81% in turbulent conditions. A similar reduction of 26.95% can also be seen at a wind speed of 15 m/s for a higher limit state. Under identical wind speeds and limit states the TMD can only reduce the fragility by 30.16% and 14.12% respectively. Throughout Table 4 the TMDI can be seen to almost always outperform the TMD across both wind speeds and for both turbulent and steady-state conditions. The steep fragility curves seen in Fig. 4, indicate that under LC1 conditions, the tower top displacements are highly dependent on wind speed.

In a similar manner, when operating in moderate met-ocean conditions with aligned wind and wave loading (LC3), the FOWT can be seen

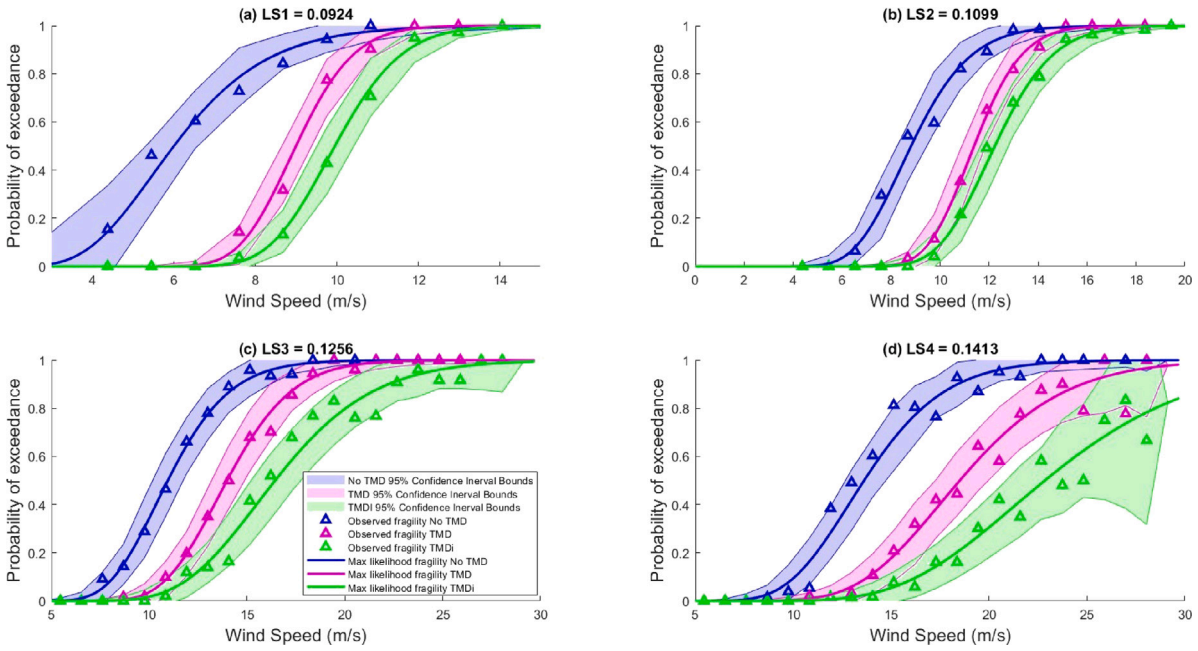

Fig. 5. LC2, Calm Met-ocean conditions, 10% turbulence intensity, Misaligned wind-wave loading, Wave significant height (0.75 m), Peak wave period (6 s).

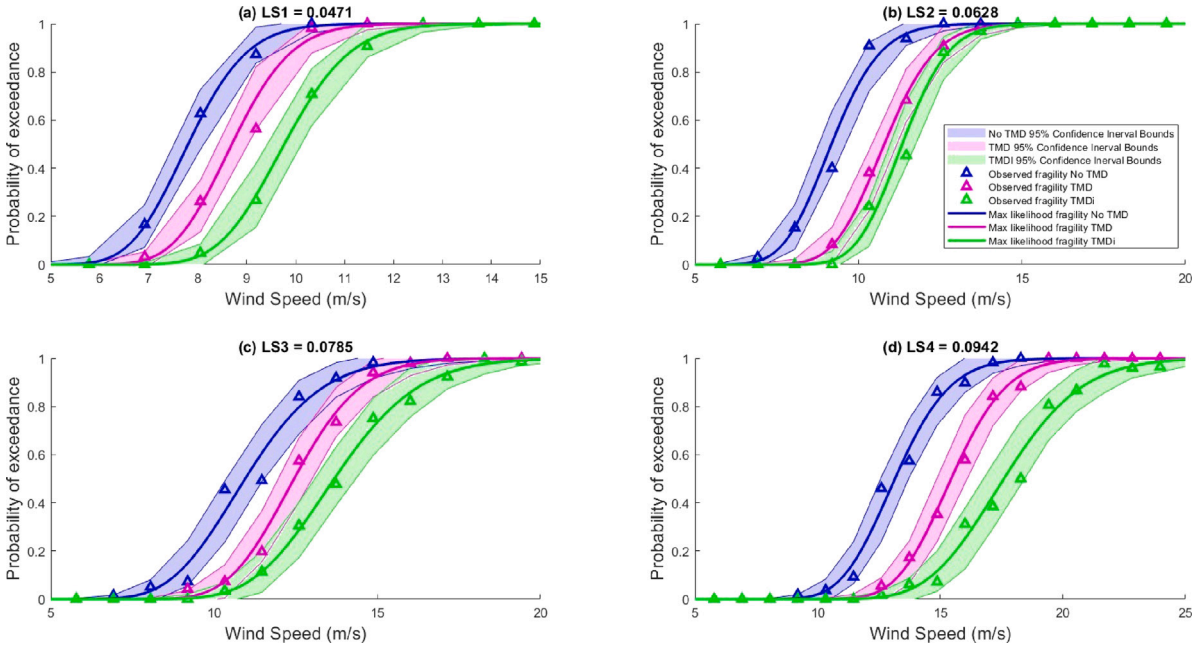

Fig. 6. LC5, Rough Met-ocean conditions, 10% turbulence intensity, Aligned wind-wave loading, Wave significant height (6 m), Peak wave period (8 s).

in Fig. 8 to experience very low maximum tower displacements. The TMDI again outperforms the TMD under these conditions shifting the fragility curves further to the right in comparison with the TMD. The superiority of the TMDI is confirmed in Table 6 where the TMDI can be seen to give reductions in fragility much greater than the TMD. At a wind speed of 11.4 m/s the TMDI gives a fragility reduction of 43.61% outperforming the TMD which at the same wind speed and the limit state provides a 29.93% fragility reduction. At a wind speed of 15 m/s under turbulent conditions, the TMDI produces a 24.42% fragility reduction for a given limit state in comparison to the TMD which only managed a 4.59% decrease. Similarly to LC1, the fragility curves under these met-ocean conditions (LC3) are again heavily dependent on wind speed represented by the steep fragility curves produced.

A response similar to LC1 and LC3 is observed when the turbine is exposed to rough met-ocean conditions with aligned wind and wave loading (LC5). The dominance of the TMDI over the TMD is again illustrated under LC5 conditions in Fig. 6 and is further reinforced by examining Table 8. At wind speeds of 11.4 m/s and 15 m/s fragility reductions of 34.67% and 4.38% are observed when a TMD is applied. For the same wind speeds and limit states the TMDI produces much greater

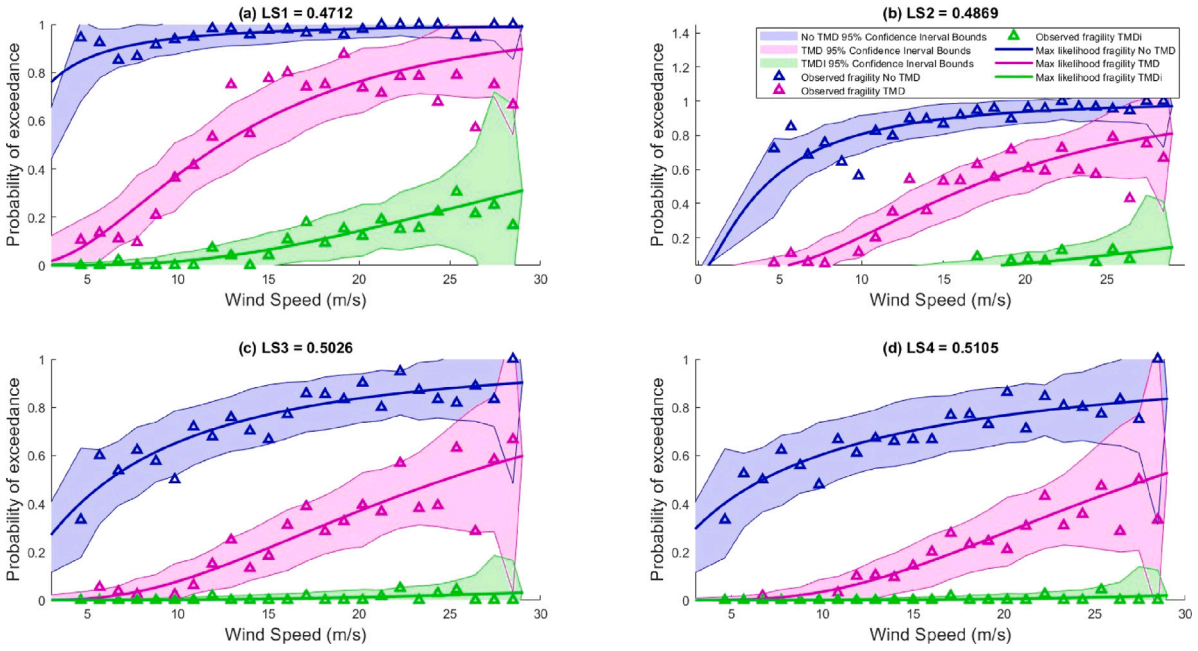

Fig. 7. LC6, Rough Met-ocean conditions, 10% turbulence intensity, Misaligned wind-wave loading, Wave significant height (6 m), Peak wave period (8s).

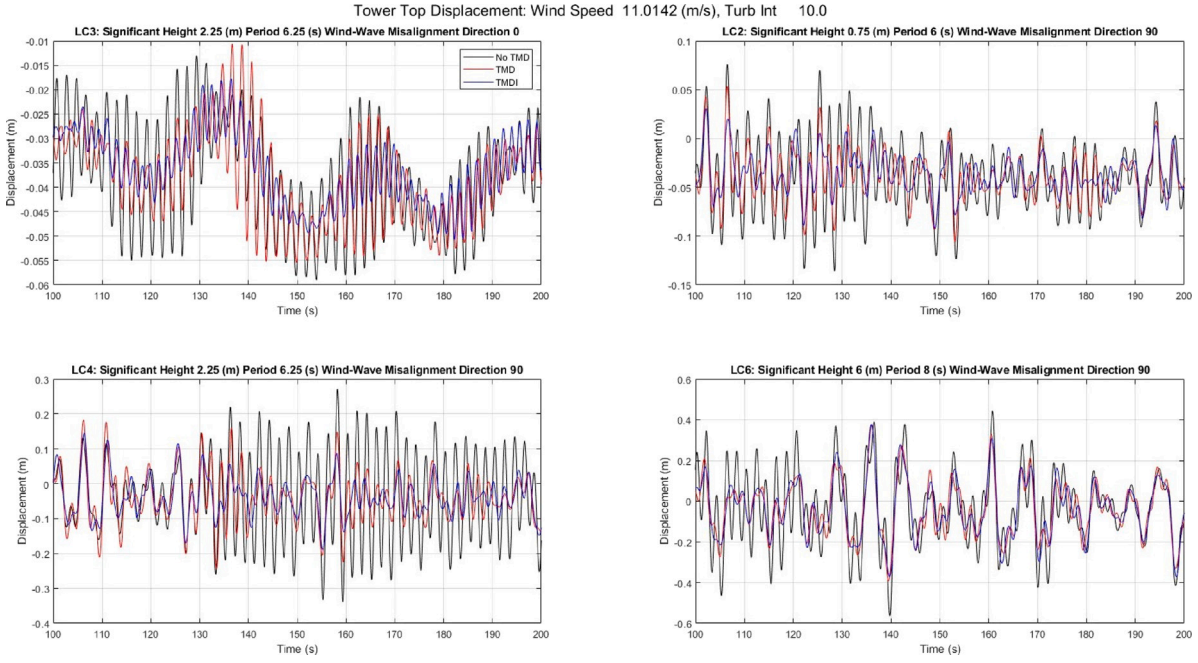

Fig. 8. Tower Top Side-To-Side Displacement Time History, 11.0142 (m/s) Wind Speed, 10% turbulence intensity.

reductions of 48.71% and 23.46% outperforming the TMD across the full range of wind speeds. Similarly to LC1 and LC3, the fragility curves produced are steep in nature highlighting the side-to-side tower top displacements dependence on wind speed.

Misaligned wind and wave loading can have a severe effect on side-to-side vibrations of FOWTs with known instabilities in this direction. For this reason, these cases have been examined in detail. For LC2, when wind-wave loading is misaligned during calm met-ocean conditions, the magnitude of tower top displacements is increased in comparison with the aligned cases'. However, as evident in Fig. 8, LC2 conditions still result in relatively low vibrational responses. The controllers can be seen in Fig. 5 to perform slightly more effectively under these conditions resulting from the increased response. The TMDI can be seen in Table 5 to again outperform the TMD at both the selected wind speeds of 11.4 m/s and 15 m/s. An example of this is for limit state 3 under turbulent conditions, the TMDI produces fragility reductions of 51.07% and 56.92% for the respective wind speeds, in comparison to 43.29% and 27.09% reductions achieved by the traditional TMD. In contrast with the aligned wind-wave cases, the fragility curves for LC2 are more gradual in nature and span over a wider range of wind speeds. The misalignment of the wave loading, which now acts in the side-to-side direction, influences the displacements of the turbine tower. The result of this can be seen as the wind speed has a slightly decreased influence on the fragility of the turbine hence producing more gradual fragility curves.

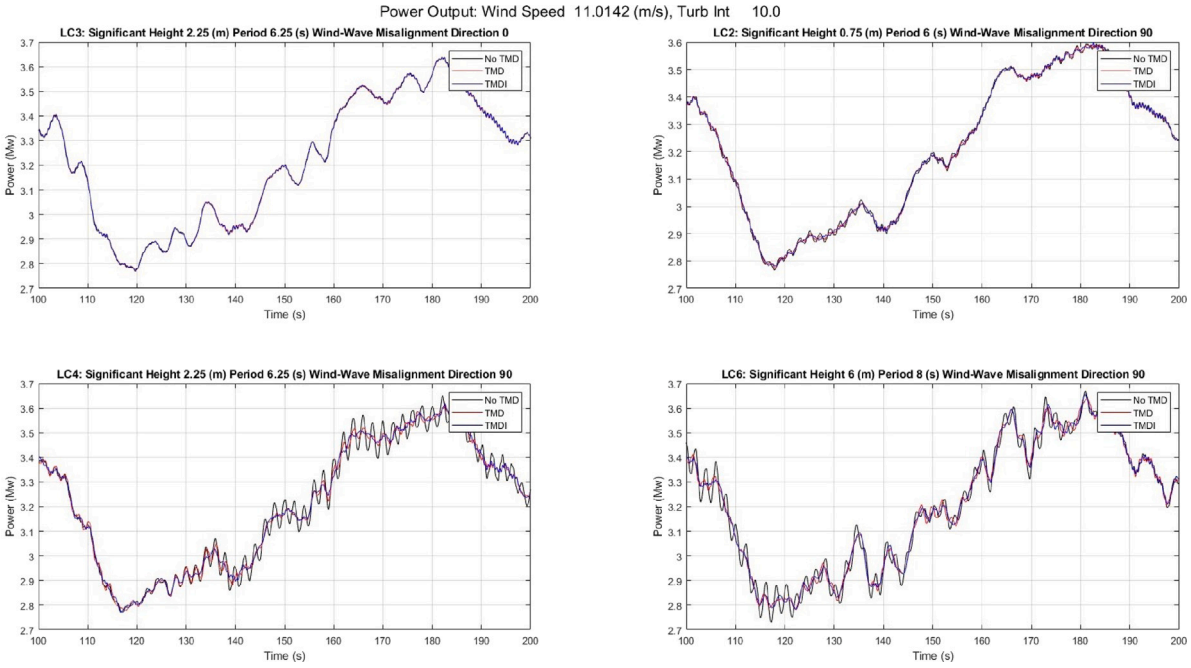

Fig. 9. Power Time History, 11.0142 (m/s) Wind Speed, 10% turbulence intensity.

Table 5
Percentage reductions in probability of limit state exceedance by controllers vs uncontrolled: Calm Met-ocean conditions, Misaligned Wind and Wave.

Calm Met-ocean conditions Misaligned Wind and Wave					
	Controller	LS1 (%)	LS2 (%)	LS3 (%)	LS4 (%)
11.4 m/s, 0% Turb	BaseLine	–	–	–	–
	TMD	−1.25	77.79	32.51	0
	TMDI	9.255	70.44	32.51	0
11.4 m/s, 10% Turb	BaseLine	–	–	–	–
	TMD	1.25	38.31	43.29	0
	TMDI	13.17	56.55	51.07	0
15 m/s, 0% Turb	BaseLine	–	–	–	–
	TMD	0	−2.11	71.11	0
	TMDI	0	22.22	74.89	0
15 m/s, 10% Turb	BaseLine	–	–	–	–
	TMD	0	1.45	27.09	0
	TMDI	0	8.33	56.92	0

Table 6
Percentage reductions in probability of limit state exceedance by controllers vs uncontrolled: Moderate Met-ocean conditions, Aligned Wind and Wave.

Moderate Met-ocean conditions Aligned Wind and Wave					
	Controller	LS1 (%)	LS2 (%)	LS3 (%)	LS4 (%)
11.4 m/s, 0% Turb	BaseLine	–	–	–	–
	TMD	0	0	1.62	0
	TMDI	99.99	−0.43	1.62	0
11.4 m/s, 10% Turb	BaseLine	–	–	–	–
	TMD	0.36	29.93	23.62	0
	TMDI	8.87	43.61	31.62	0
15 m/s, 0% Turb	BaseLine	–	–	–	–
	TMD	0	0	82.19	0
	TMDI	0	0.69	89.09	0
15 m/s, 10% Turb	BaseLine	–	–	–	–
	TMD	0	0.26	4.59	0
	TMDI	0.0012	0.48	24.42	0

Table 7
Percentage reductions in probability of limit state exceedance by controllers vs uncontrolled: Moderate Met-ocean conditions, Misaligned Wind and Wave.

Moderate Met-ocean conditions Misaligned Wind and Wave					
	Controller	LS1 (%)	LS2 (%)	LS3 (%)	LS4 (%)
11.4 m/s, 0% Turb	BaseLine	–	–	–	–
	TMD	58.62	69.16	44.64	0
	TMDI	92.74	71.14	45.08	0
11.4 m/s, 10% Turb	BaseLine	–	–	–	–
	TMD	53.26	63.16	49.98	0
	TMDI	91.12	72.10	52.13	0
15 m/s, 0% Turb	BaseLine	–	–	–	–
	TMD	5.15	61.40	59.08	0
	TMDI	98.54	87.20	61.49	0
15 m/s, 10% Turb	BaseLine	–	–	–	–
	TMD	26.27	54.86	57.10	0.0037
	TMDI	94.86	85.26	66.90	0.0037

Table 8
Percentage reductions in probability of limit state exceedance by controllers vs uncontrolled: Rough Met-ocean conditions, Aligned Wind and Wave.

Rough Met-ocean conditions Aligned Wind and Wave					
	Controller	LS1 (%)	LS2 (%)	LS3 (%)	LS4 (%)
11.4 m/s, 0% Turb	BaseLine	–	–	–	–
	TMD	0.17	63.49	10.59	0
	TMDI	0	59.80	10.69	0
11.4 m/s, 10% Turb	BaseLine	–	–	–	–
	TMD	0.62	26.86	34.67	0
	TMDI	7.71	43.29	48.71	0
15 m/s, 0% Turb	BaseLine	–	–	–	–
	TMD	0	0	69.256	0
	TMDI	0	0.0014	99.63	0
15 m/s, 10% Turb	BaseLine	–	–	–	–
	TMD	0	0.18	4.38	0
	TMDI	0	0.23	23.46	0

Table 9
Percentage reductions in probability of limit state exceedance by controllers vs uncontrolled: Rough Met-ocean conditions, Misaligned Wind and Wave.

Rough Met-ocean conditions Misaligned Wind and Wave					
	Controller	LS1 (%)	LS2 (%)	LS3 (%)	LS4 (%)
11.4 m/s, 0% Turb	BaseLine	–	–	–	–
	TMD	0.54	14.67	45.17	54.257
	TMDI	0.64	70.15	91.95	59.097
11.4 m/s, 10% Turb	BaseLine	–	–	–	–
	TMD	0.54	13.52	50.09	58.10
	TMDI	0.88	60.59	92.64	63.70
15 m/s, 0% Turb	BaseLine	–	–	–	–
	TMD	0.35	8.47	30.07	55.32
	TMDI	0.41	60.90	93.62	64.28
15 m/s, 10% Turb	BaseLine	–	–	–	–
	TMD	0.37	8.15	35.64	56.78
	TMDI	0.62	49.04	90.41	70.20

As can be seen in Fig. 8, the tower top displacements under LC4 conditions have increased dramatically in comparison with the calm met-ocean condition (LC2). The effects of wind-wave misalignment can be more evidently seen in fragility curves produced by moderate met-ocean conditions with wind-wave misalignment (LC4). The increased wave loading in the side-to-side direction induces larger tower displacements and thus has a large influence on the fragility curves. This effect is increasingly evident for higher limit states where higher responses are observed. The increased response allows the controllers to demonstrate their capacity to suppress vibrations. Reductions of fragility of +60% can be seen in Table 7 across the range of wind speeds and limit states for the TMD. The full effect of the TMDI can now be seen as it produces fragility reductions of +80%. The fragility curves produced by the misaligned wind-wave loading are much less steep in comparison with the aligned conditions. The fragility curves span over a wider range of wind speeds due to the increased influence of misaligned wave loading on the towers displacement. Wind loading now has a less dramatic impact when compared to LC1, LC3 and LC5 when wind and wave loading's are aligned.

The influence of wind-wave misalignment is heightened during rough met-ocean conditions (LC6). Fig. 8 demonstrates that the responses of the turbine are greatly increased in comparison with the

Table 10
Percentage reductions of maximum tower top side-to-side displacements by controllers vs uncontrolled.

Wave Conditions	Control (%)	0% Turb (%)	10% Turb (%)
Calm Met-ocean Aligned	Baseline	–	–
	TMD	13.38	17.912
	TMDI	14.31	26.34
Calm Met-ocean misaligned	Baseline	–	–
	TMD	19.59	13.175
	TMDI	23.99	13.067
Moderate Met-ocean Aligned	Baseline	–	–
	TMD	11.68	16.78
	TMDI	13.14	21.00
Moderate Met-ocean misaligned	Baseline	–	–
	TMD	19.59	13.16
	TMDI	22.54	25.59
Rough Met-ocean Aligned	Baseline	–	–
	TMD	15.034	6.49
	TMDI	32.55	23.05
Rough Met-ocean Misaligned	Baseline	–	–
	TMD	18.26	15.60
	TMDI	22.52	26.35

Table 11
Percentage increase in tower top side-to-side displacements when subjected to misaligned wind-wave vs aligned wind-wave.

		Hs (m)	Tp (s)	Misalignment	Baseline (%)	TMD (%)	TMDI (%)
0% Turb	LC1	0.75	6	0°	–	–	–
	LC2	0.75	6	90°	86.71	73.39	65.62
10% Turb	LC1	0.75	6	0°	–	–	–
	LC2	0.75	6	90°	0.45	10.16	18.56
0% Turb	LC3	2.25	6.25	0°	–	–	–
	LC4	2.25	6.25	90°	266.96	189.3	183.38
10% Turb	LC3	2.25	6.25	0°	–	–	–
	LC4	2.25	6.25	90°	95.14	103.60	83.79
0% Turb	LC5	6	8	0°	–	–	–
	LC6	6	8	90°	371.1	353.17	441.1
10% Turb	LC5	6	8	0°	–	–	–
	LC6	6	8	90°	247.99	214.1	233.05

aligned conditions (LC3). The TMDI greatly outperforms the TMD in these conditions as depicted in Fig. 7. This is reinforced in Table 9 where the TMDI can be seen to decrease fragility by +90% in comparison to the TMD which produces fragility reductions of +60%. Similar to LC4, the fragility curves are much less steep in nature as the misaligned wave loading becomes the dominant force influencing tower top displacements.

The influence of misaligned wind-wave loading on FOWT's is evident in Table 11 which is provided to demonstrate the impact that wind-wave misalignment has on the response of the FOWT tower. It can be seen that for moderate and rough conditions the displacements are largely increased when wind and wave loading is misaligned. This demonstrates the importance of including misalignment assessments in the design of FOWTs.

The importance of devices such as TMDI's and TMD's in misaligned conditions is furthered in Table 10 which shows the percentage by which the maximum displacements are decreased by the controllers. From viewing this table it can be seen that the TMDI provides larger vibration mitigation for the same damper mass. This can be seen in particular for conditions where the FOWT response is large such as in misaligned rough met-ocean conditions (LC6).

The inclusion of a damping devices extends beyond structural aspects as seen in Fig. 9 which presents the power output time history of the wind turbine. The sample of time histories is selected for a wind speed of 11.0142 m/s (i.e below rated wind speed) with 10% turbulence intensity. The TMD and TMDI can be seen to reduce fluctuations in power output. The TMDI once again outperforms the TMD providing a much smoother power output.

4.1. A note on confidence intervals

When analysing a structural system, it is important to consider all potential sources of uncertainty that could affect the system's performance, such as material properties, design assumptions, and environmental loads. In this context, we have provided 95% confidence intervals on the estimated fragility curves to ensure that the results and conclusions we have drawn are statistically significant. The confidence intervals can be seen in the fragility curves in Figs. 4–7. In Figs. 4–6 it can be seen that there are some overlapping confidence intervals on the fragility curves. The overlap appears to occur mainly for low wind speeds in calm met ocean conditions (Figs. 4 and 5). In these conditions the structure is not excited as dynamically as in rough met ocean conditions and as such there is less improvement apparent between the TMD and TMDIs. It is interesting to note that in Fig. 6 there is a smaller overlap between the confidence intervals within the operating regime of the wind turbine and in Fig. 7 there is no overlap. Figs. 6 and 7 correspond to rough met ocean conditions, this suggests that the difference observed between the different cases (uncontrolled, TMD, TMDI) is unlikely to be due to chance and is likely due to a statistically significant difference between the groups.

Generally, when comparing two parameter statistics, if the 95% confidence intervals do not overlap, then the null hypothesis of zero difference between the parameters will be rejected at the 0.05 level and the statistics are significantly different. However, the converse is not true. That is if the 95% confidence intervals do overlap, then we cannot determine whether the null hypothesis of zero difference between the parameters will be rejected at the 0.05 level. It is necessary to perform the statistical test for this null hypothesis using the appropriate test

statistic or compute the confidence interval of the difference. The fragility curves in Figs. 4–6 in this paper display some overlapping confidence intervals. As mentioned, for the overlapping confidence intervals, it is not straightforward to conclude if the overlapping statistics are significantly different. However, from Figs. 4–6 the overlap can be observed between the "No TMD" and "TMD" cases and the "TMD" and "TMDI" cases. Therefore, further statistical tests are required to determine the statistical difference between the "No TMD" and "TMD" cases and the "TMD" and the "TMDI" cases. The absence of overlap between the "No TMD" and the "TMDI" cases clearly demonstrates that the enhancement of reliability offered by the TMDI is statistically significant. Also, the fact that in all of the 36,000 simulations performed in this paper the TMDI has always outperformed TMDs (which is also evident from the scattered data points used to fit the fragility curves) is significant.

5. Conclusion

In this paper, the use of a TMDI for vibration control of floating offshore wind turbine towers was demonstrated and its improvements in reliability were investigated. A fully coupled 23 degrees of freedom numerical model was implemented to run 36,000 simulations over a range of wind speeds and environmental conditions. Fragility curves for the turbine produced via the Maximum Likelihood Estimation (MLE) were used to assess the performances of a traditional TMD in comparison with the novel TMDI. Both of the controllers displayed large reductions in fragility hence improving the reliability of the turbine. The TMDI outperformed the traditional TMD across the full range of wind speeds and loading conditions, producing significantly increased vibration mitigation for the same damper mass. The largest reductions were observed when wind and wave loading were misaligned. During rough met-ocean conditions, a maximum fragility reduction of 92.64% was identified at the turbine's rated wind speed.

The important conclusions are

1. The TMDI offers great potential in vibration mitigation for floating offshore wind turbine towers. This novel damper performs significantly better than the traditional TMD for the same damper mass. Since the space available inside a wind turbine tower is very limited, the reduction in damper mass is an extremely beneficial and practical advantage over classical TMDs for application in FOWTs.
2. TMDIs can achieve impressive improvements in the reliability of FOWT towers. Improvements of over 90% were demonstrated for rough met-ocean conditions with wind-wave misalignment.
3. Wind-wave misalignment has a significant impact on the magnitude of the side-to-side vibration response of FOWTs. Under the same wind and wave loading conditions, the displacements experienced by a turbine can be increased by over 400% when the wind and waves are misaligned.
4. By installing a TMDI in a turbine tower, the vibration response of the tower will be decreased having a number of important effects: the reliability of the turbine will be increased hence decreasing costly downtimes during repairs, accelerations in the nacelle will be reduced protecting sensitive components and decreased vibration response will allow for a reduction of fluctuations in power production. By combining all these effects turbines will produce better quality power for longer periods thus decreasing their LCOE.

CRediT authorship contribution statement

Breiffni Fitzgerald: Conceptualization, Methodology, Software, Supervision, Writing – review & editing. **James McAuliffe:** Data curation, Writing – original draft. **Shubham Baisthakur:** Software. **Saptarshi Sarkar:** Writing – review & editing, Software.

Declaration of competing interest

The authors declare that they have no known competing financial interests or personal relationships that could have appeared to influence the work reported in this paper.

Acknowledgments

The Funding for this research was provided by the Sustainable Energy Authority of Ireland (SEAI) under the WindLEDeRR project, grant number RDD 601.

The authors are thankful for the support received.

Appendix A

Degrees of freedom:

q_{Sg}	Platform surge
q_{Sw}	Platform sway
q_{Hv}	Platform heave
q_{R}	Platform roll
q_{P}	Platform pitch
q_{Y}	Platform yaw
q_{TFA1}	First tower fore-aft bending mode
q_{TFA2}	Second tower fore-aft bending mode
q_{TSS1}	First tower side-to-side bending mode
q_{TSS2}	Second tower side-to-side bending mode
q_{yaw}	Nacelle yaw
q_{GeAz}	Generator azimuth angle
q_{DrTr}	Drive-train torsional flexibility
q_{BiF1}	First flapwise bending mode for ith blade
q_{BiF2}	Second flapwise bending mode for ith blade
q_{BiE1}	First edgewise bending mode for ith blade
q_{D}	Damper

Appendix B. Benchmarking against FAST v8

All of the numerical codes used to model the FOWT in this paper are developed in MATLAB®. In this section, the 22 DOF floating offshore wind turbine model presented in this study is validated against the state-of-the-art wind turbine simulator FAST [51] using code-to-code comparison. The spar type FOWT multi-body dynamic model developed theoretically is instantiated using the details provided from the NREL 5MW baseline offshore wind turbine [52]. The offshore wind turbine is simulated under a steady (rated) wind speed of 11.4 m/s in still water for verification purposes. The aerodynamic loads are calculated using the Blade Element Momentum Theory (BEM). The verification results for the primary structural responses are shown in Fig. B.10. The other responses of the offshore wind turbine are provided in Figs. B.11. A comparison of the time histories after the initial transient phase (50 secs) is presented in terms of the mean, standard deviation, and max/min values in Table B.12. The numerical results compare satisfactorily with FAST [51] which numerically verifies the developed multi-body model using Kane's method.

The responses of the floating offshore wind turbine tower, blades, nacelle, and low-speed shaft match very well with the ones obtained from FAST [51] as shown in Fig. B.10. However, minor dissimilarities are observed in the platform motion in Fig. B.11. A phase shift can be observed in the floating platform response time histories. While FAST [51] includes radiation forces from the linear potential flow theory together with viscous drag forces from Morison's equation, the model derived here only includes the viscous drag forces from Morison's equation. The difference in the resulting hydrodynamic damping forces manifests a phase shift in the response time histories. It is also noteworthy that the degrees of freedom that are subjected to lower levels of hydrodynamic damping like the platform surge, the platform heaves or reaches steady state quickly like platform pitch and

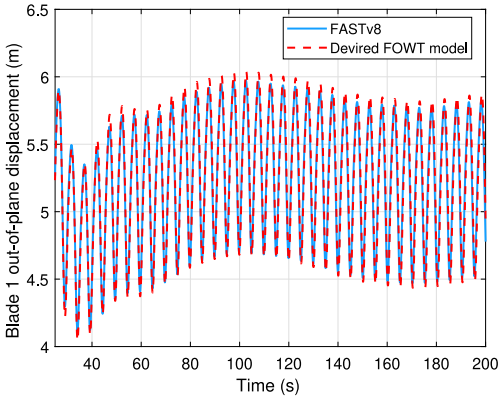

(a) Blade 1 out-of-plane displacement

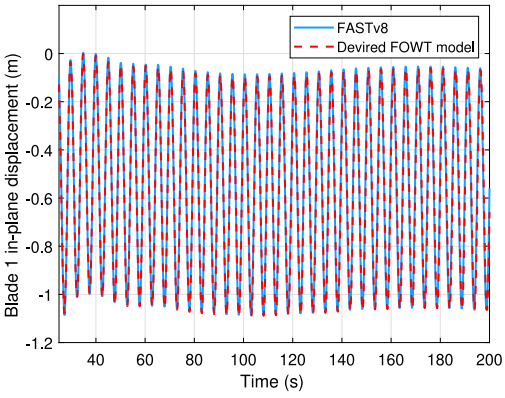

(b) Blade 1 in-plane displacement

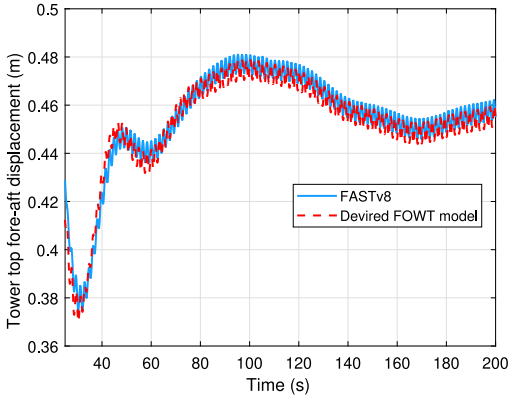

(c) Tower top fore-aft displacement

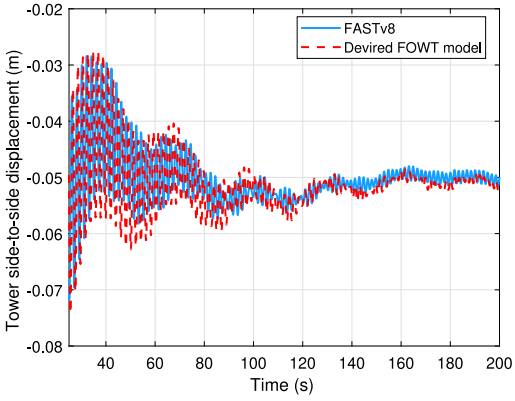

(d) Tower to side-to-side displacement

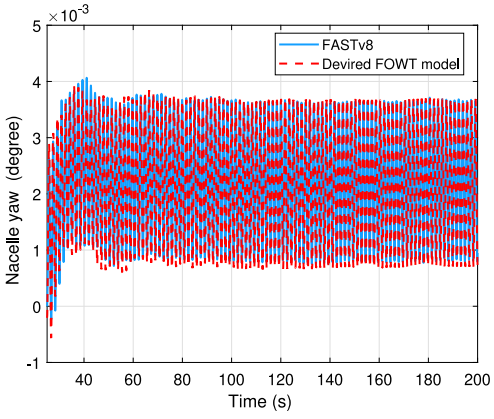

(e) Nacelle yaw rotation

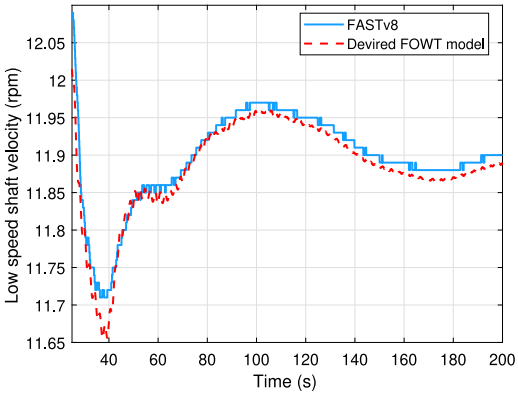

(f) Low speed shaft speed

Fig. B.10. Model verification: motion of the floating offshore wind turbine.

the platform yaw is less affected by this phase shift. The degrees of freedom most affected by this phase shift are the platform sway and roll degrees of freedom. However, it can be observed that the mean and the frequency content of all of the responses match very well with FAST [51] which is most important from a dynamic analysis point of view.

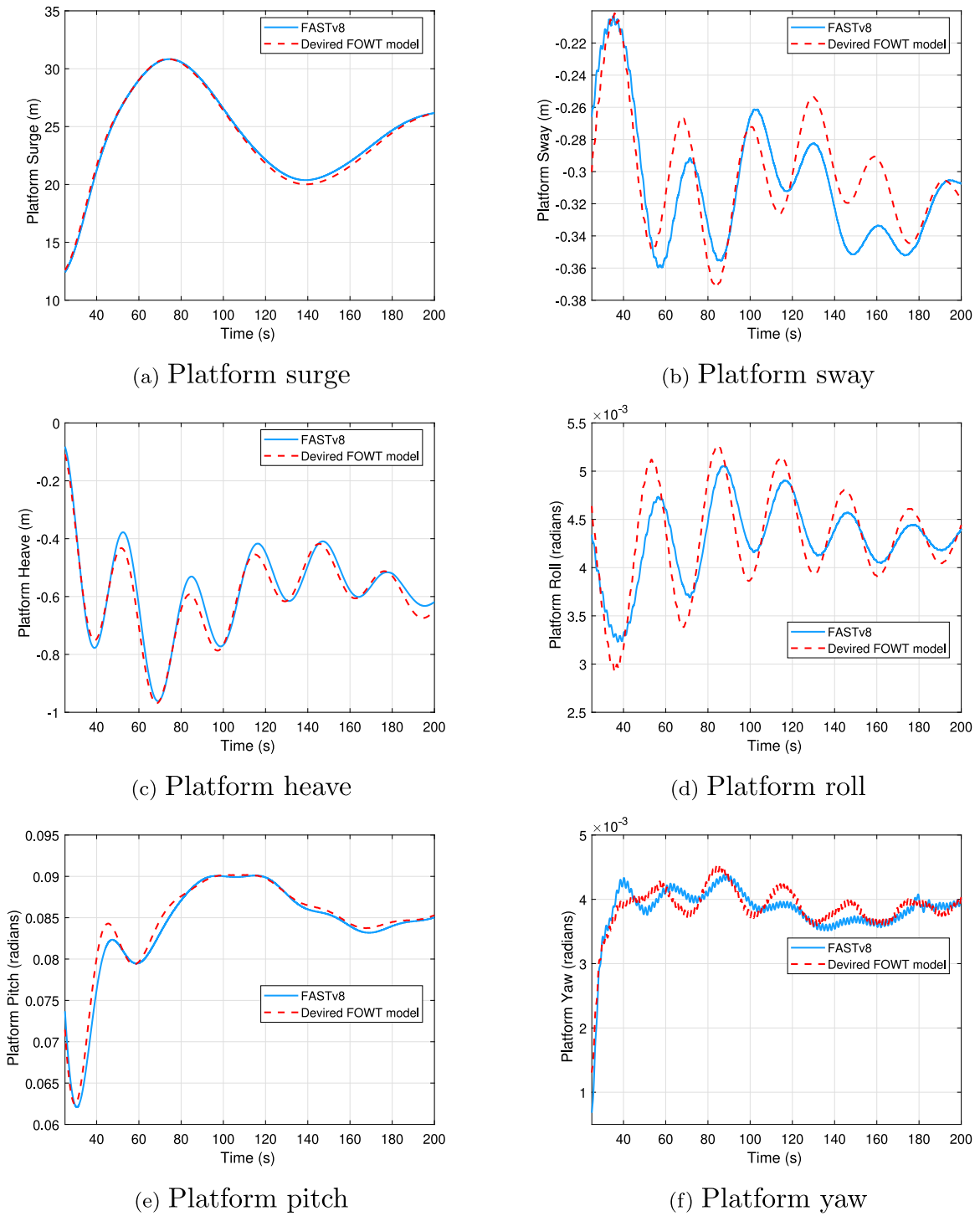

(a) Platform surge

(b) Platform sway

(c) Platform heave

(d) Platform roll

(e) Platform pitch

(f) Platform yaw

Fig. B.11. Model verification: motion of the floating offshore wind turbine platform.

Table B.12
Comparison of response statistic between FAST and the 22 DOF model.

Response	Mean		Min		Max		Std.	
	FAST	DM	FAST	DM	FAST	DM	FAST	DM
Blade OOP displacement (m)	5.283	5.296	4.396	4.366	5.971	6.037	0.448	0.477
Blade IP displacement (m)	−0.559	−0.565	−1.085	−1.090	−0.038	−0.046	0.354	0.353
Tower-top FA displacement (m)	0.460	0.458	0.436	0.431	0.481	0.478	0.011	0.011
Tower-top SS displacement (m)	−0.051	−0.051	−0.058	−0.062	−0.040	−0.040	0.003	0.003

(*continued on next page*)

Table B.12 (*continued*).

Response	Mean		Min		Max		Std.	
	FAST	DM	FAST	DM	FAST	DM	FAST	DM
Nacelle yaw angle (°)	2.2E−3	2.2E−3	7.1E−4	6.1E−4	3.8E−3	3.8E−3	1.0E−3	1.0E−3
Rotor speed (RPM)	11.910	11.899	11.840	11.834	11.970	11.959	0.035	0.035
Platform surge (m)	25.075	24.872	20.380	20.009	30.830	30.837	3.430	3.564
Platform sway (m)	−0.319	−0.309	−0.359	−0.372	−0.261	−0.253	0.026	0.027
Platform heave (m)	−0.589	−0.611	−0.961	−0.968	−0.377	−0.417	0.133	0.131
Platform roll (rad)	4.4E−3	4.4E−3	3.7E−3	3.4E−3	5.1E−3	5.3E−3	2.95E−4	4.45E−4
Platform pitch (rad)	0.085	0.086	0.079	0.079	0.090	0.090	3.1E−3	2.9E−3
Platform yaw (rad)	3.9E−3	3.9E−3	3.5E−3	3.6E−3	4.4E−3	4.5E−3	2.1E−4	2.1E−4

References

[1] P. Bojek, IEA (2021) Wind Power, IEA, Paris, Tech. Rep., International Energy Agency, 2021.

[2] M. Taylor, IRENA (2021) Renewable Power Generation Costs in 2020, International Renewable Energy Agency, Abu Dhabi, Tech. Rep., International Renewable Energy Agenc, 2020.

[3] G. Van Kuik, J. Peinke, R. Nijssen, D. Lekou, J. Mann, J.N. Sørensen, C. Ferreira, J.-W. van Wingerden, D. Schlipf, P. Gebraad, et al., Long-term research challenges in wind energy–a research agenda by the European Academy of Wind Energy, Wind Energy Sci. 1 (1) (2016) 1–39.

[4] L. Dueñas-Osorio, B. Basu, Unavailability of wind turbines due to wind-induced accelerations, Eng. Struct. 30 (4) (2008) 885–893.

[5] A. Teramura, S. Inaba, A. Kawaguchi, S. Kimura, Y. Takashino, Development of vibration control device for tower of wind power generator; furyoku hatsuden tower yo seishin sochi no kaihatsu, Obayashi-Gumi Gijutsu Kenkyusho-Ho (Report of the Engineering Research Laboratory Obayashi-Gumi) (2000).

[6] P. Murtagh, A. Ghosh, B. Basu, B. Broderick, Passive control of wind turbine vibrations including blade/tower interaction and rotationally sampled turbulence, Wind Energy Int. J. Progr. Appl. Wind Power Convers. Technol. 11 (4) (2008) 305–317.

[7] M.A. Lackner, M.A. Rotea, Passive structural control of offshore wind turbines, Wind Energy 14 (3) (2011) 373–388.

[8] Y. Si, H.R. Karimi, H. Gao, Modeling and parameter analysis of the OC3-hywind floating wind turbine with a tuned mass damper in nacelle, J. Appl. Math. 2013 (2013).

[9] Y. Si, H.R. Karimi, H. Gao, Modelling and optimization of a passive structural control design for a spar-type floating wind turbine, Eng. Struct. 69 (2014) 168–182.

[10] G.M. Stewart, M.A. Lackner, The impact of passive tuned mass dampers and wind–wave misalignment on offshore wind turbine loads, Eng. Struct. 73 (2014) 54–61.

[11] C. Sun, V. Jahangiri, Bi-directional vibration control of offshore wind turbines using a 3D pendulum tuned mass damper, Mech. Syst. Signal Process. 105 (2018) 338–360.

[12] J.O. Martin del Campo, A. Pozos-Estrada, O. Pozos-Estrada, Development of fragility curves of land-based wind turbines with tuned mass dampers under cyclone and seismic loading, Wind Energy 24 (7) (2021) 737–753.

[13] B. Fitzgerald, B. Basu, Vibration control of wind turbines: recent advances and emerging trends, Int. J. Sustain. Mater. Struct. Syst. 4 (2020) 347–372.

[14] M.A. Lackner, M.A. Rotea, Structural control of floating wind turbines, Mechatronics 21 (4) (2011) 704–719.

[15] B. Fitzgerald, B. Basu, S.R. Nielsen, Active tuned mass dampers for control of in-plane vibrations of wind turbine blades, Struct. Control Health Monit. 20 (12) (2013) 1377–1396.

[16] B. Fitzgerald, S. Sarkar, A. Staino, Improved reliability of wind turbine towers with active tuned mass dampers (ATMDs), J. Sound Vibr. 419 (2018) 103–122.

[17] J. Arrigan, V. Pakrashi, B. Basu, S. Nagarajaiah, Control of flapwise vibrations in wind turbine blades using semi-active tuned mass dampers, Struct. Control Health Monit. 18 (8) (2011) 840–851.

[18] H.R. Karimi, M. Zapateiro, N. Luo, Semiactive vibration control of offshore wind turbine towers with tuned liquid column dampers using H output feedback control, in: 2010 IEEE International Conference on Control Applications, IEEE, 2010, pp. 2245–2249.

[19] A.F. Mensah, L. Dueñas-Osorio, Improved reliability of wind turbine towers with tuned liquid column dampers (TLCDs), Struct. Saf. 47 (2014) 78–86.

[20] S. Sarkar, A. Chakraborty, Optimal design of semiactive MR-TLCD for along-wind vibration control of horizontal axis wind turbine tower, Struct. Control Health Monit. 25 (2) (2018) e2083.

[21] M.C. Smith, Synthesis of mechanical networks: the inerter, IEEE Trans. Automat. Control 47 (10) (2002) 1648–1662.

[22] L. Marian, A. Giaralis, Optimal design of a novel tuned mass-damper-inerter (TMDI) passive vibration control configuration for stochastically support-excited structural systems, Probabilist. Eng. Mech. 38 (2014) 156–164.

[23] Y. Hu, M.Z. Chen, Inerter-based passive structural control for load mitigation of wind turbines, in: 2017 29th Chinese Control and Decision Conference, CCDC, IEEE, 2017, pp. 3056–3061.

[24] Y. Hu, J. Wang, M.Z. Chen, Z. Li, Y. Sun, Load mitigation for a barge-type floating offshore wind turbine via inerter-based passive structural control, Eng. Struct. 177 (2018) 198–209.

[25] R. Ma, K. Bi, H. Hao, Mitigation of heave response of semi-submersible platform (SSP) using tuned heave plate inerter (THPI), Eng. Struct. 177 (2018) 357–373.

[26] S. Sarkar, B. Fitzgerald, Vibration control of spar-type floating offshore wind turbine towers using a tuned mass-damper-inerter, Struct. Control Health Monit. 27 (1) (2020) e2471.

[27] R. Zhang, Z. Zhao, K. Dai, Seismic response mitigation of a wind turbine tower using a tuned parallel inerter mass system, Eng. Struct. 180 (2019) 29–39.

[28] D. Villoslada, M. Santos, M. Tomás-Rodríguez, Inerter-based passive structural control for barge floating offshore wind turbines, IFAC-PapersOnLine 53 (2) (2020) 12358–12363.

[29] Z. Zhang, B. Fitzgerald, Tuned mass-damper-inerter (TMDI) for suppressing edgewise vibrations of wind turbine blades, Eng. Struct. 221 (2020) 110928.

[30] Z. Zhang, T.G. Larsen, Optimal calibration of the rotational inertia double tuned mass damper (RIDTMD) for rotating wind turbine blades, J. Sound Vibr. 493 (2021) 115827.

[31] H. Garrido, O. Curadelli, D. Ambrosini, Improvement of tuned mass damper by using rotational inertia through tuned viscous mass damper, Eng. Struct. 56 (2013) 2149–2153.

[32] Z. Zhang, C. Høeg, Inerter-enhanced tuned mass damper for vibration damping of floating offshore wind turbines, Ocean Eng. 223 (2021) 108663.

[33] R. Zhang, Y. Cao, K. Dai, Response control of wind turbines with ungrounded tuned mass inerter system (TMIS) under wind loads, Wind Struct. 32 (6) (2021) 573–586.

[34] M.Z. Chen, Z. Li, H. Wang, Y. Hu, Seismic response mitigation of a wind turbine via inerter-based structural control, Bullet. Earthq. Eng. (2021) 1–28.

[35] T. Sun, Z. Zhang, Optimal control and performance evaluation of an inerter-based point absorber wave energy converter, Ocean Eng. 259 (2022) 111883.

[36] S. Sarkar, B. Fitzgerald, Fluid inerter for optimal vibration control of floating offshore wind turbine towers, Eng. Struct. 266 (2022) 114558.

[37] C. Yuan, Y. Xie, J. Li, W. Bai, H. Li, Influence of the number of ground motions on fragility analysis of 5 MW wind turbines subjected to aerodynamic and seismic loads interaction, Energies 15 (6) (2022) 2094.

[38] A. Quilligan, A. O'Connor, V. Pakrashi, Fragility analysis of steel and concrete wind turbine towers, Eng. Struct. 36 (2012) 270–282.

[39] D.H. Kim, S.G. Lee, I.K. Lee, Seismic fragility analysis of 5 MW offshore wind turbine, Renew. Energy 65 (2014) 250–256.

[40] M.-A. Asareh, W. Schonberg, J. Volz, Fragility analysis of a 5-MW NREL wind turbine considering aero-elastic and seismic interaction using finite element method, Finite Elem. Anal. Des. 120 (2016) 57–67.

[41] R. Mo, H. Kang, M. Li, X. Zhao, Seismic fragility analysis of monopile offshore wind turbines under different operational conditions, Energies 10 (7) (2017) 1037.

[42] C. Yuan, J. Chen, J. Li, Q. Xu, Fragility analysis of large-scale wind turbines under the combination of seismic and aerodynamic loads, Renew. Energy 113 (2017) 1122–1134.

[43] A. Hemmati, E. Oterkus, N. Barltrop, Fragility reduction of offshore wind turbines using tuned liquid column dampers, Soil Dyn. Earthq. Eng. 125 (2019) 105705.

[44] H. Zuo, K. Bi, H. Hao, Y. Xin, J. Li, C. Li, Fragility analyses of offshore wind turbines subjected to aerodynamic and sea wave loadings, Renew. Energy 160 (2020) 1269–1282.

[45] J.M. Del Campo, A. Pozos-Estrada, Multi-hazard fragility analysis for a wind turbine support structure: An application to the Southwest of Mexico, Eng. Struct. 209 (2020) 109929.

[46] C. Yuan, J. Li, J. Chen, Q. Xu, Y. Xie, Study on the influence of baseline control system on the fragility of large-scale wind turbine considering seismic-aerodynamic combination, Adv. Civ. Eng. 2020 (2020).

[47] S. Sarkar, B. Fitzgerald, Use of Kane's method for multi-body dynamic modelling and control of spar-type floating offshore wind turbines, Energies 14 (20) (2021) 6635.

[48] M. Hall, MoorDyn user's guide, Orono ME Dep. Mech. Eng. Univ. Maine (2015).

[49] T.R. Kane, D.A. Levinson, Dynamics, Theory and Applications, McGraw Hill, 1985.
[50] S. Sarkar, L. Chen, B. Fitzgerald, B. Basu, Multi-resolution wavelet pitch controller for spar-type floating offshore wind turbines including wave-current interactions, J. Sound Vibr. (2020) 115170.
[51] J. Jonkman, M. Buhl Jr., FAST user's guide, 2005, National Renewable Energy Laboratory, Golden, CO, Technical Report No. NREL/EL-500-38230.
[52] J. Jonkman, S. Butterfield, W. Musial, G. Scott, Definition of a 5-MW Reference Wind Turbine for Offshore System Development, Tech. Rep., National Renewable Energy Lab.(NREL), Golden, CO (United States), 2009.
[53] J.M. Jonkman, Definition of the Floating System for Phase IV of OC3, 2010.
[54] MATLAB, Version 9.4.0 (R2018a), The MathWorks Inc., Natick, Massachusetts, 2018.
[55] A. Ghosh, B. Basu, A closed-form optimal tuning criterion for TMD in damped structures, Struct. Control Health Monit. (ISSN: 1545-2263) 14 (4) (2007) 681–692, http://dx.doi.org/10.1002/stc.176.
[56] N. Hoang, Y. Fujino, P. Warnitchai, Optimal tuned mass damper for seismic applications and practical design formulas, Eng. Struct. 30 (3) (2008) 707–715.
[57] R. Luft, Optimal tuned mass dampers for buildings, J. Struct. Div., ASCE 105 (1979) 2766–2772.
[58] A. Giaralis, F. Petrini, Wind-induced vibration mitigation in tall buildings using the tuned mass-damper-inerter, J. Struct. Eng. 143 (9) (2017) 04017127.
[59] B.J. Jonkman, TurbSim user's guide: Version 1.50, Tech. Rep., National Renewable Energy Lab.(NREL), Golden, CO (United States), 2009.
[60] IEC 61400-1: Wind turbines part 1: Design requirements, Int. Electrotech. Commission (2005).
[61] S.A. Ning, A simple solution method for the blade element momentum equations with guaranteed convergence, Wind Energy 17 (9) (2014) 1327–1345.
[62] W.J. Pierson Jr., L. Moskowitz, A proposed spectral form for fully developed wind seas based on the similarity theory of SA Kitaigorodskii, J. Geophys. Res. 69 (24) (1964) 5181–5190.
[63] J.W. Baker, Efficient analytical fragility function fitting using dynamic structural analysis, Earthq. Spectra 31 (1) (2015) 579–599.
[64] K. Trevlopoulos, I. Zentner, Seismic fragility curve assessment based on synthetic ground motions with conditional spectra, Pure Appl. Geophys. 177 (5) (2020) 2375–2390.